Magn Reson Mater Phy
DOI 10.1007/s10334-012-0318-7

RESEARCH ARTICLE

Fully refocused multi-shot spatiotemporally encoded MRI: robust imaging in the presence of metallic implants

Noam Ben-Eliezer · Eddy Solomon · Elad Harel · Nava Nevo · Lucio Frydman

Received: 13 December 2011 / Revised: 26 April 2012 / Accepted: 27 April 2012

Abstract
Object An approach has been recently introduced for acquiring arbitrary 2D NMR spectra or images in a single scan, based on the use of frequency-swept RF pulses for the sequential excitation and acquisition of the spins response. This spatiotemporal-encoding (*SPEN*) approach enables a unique, voxel-by-voxel refocusing of all frequency shifts in the sample, for all instants throughout the data acquisition. *The present study investigates the use of this full-refocusing aspect of SPEN-based imaging in the multi-shot MRI of objects, subject to sizable field inhomogeneities that complicate conventional imaging approaches.*
Materials and methods 2D MRI experiments were performed at 7 T on phantoms and on mice in vivo, focusing on imaging in proximity to metallic objects. Fully refocused SPEN-based spin echo imaging sequences were implemented, using both Cartesian and back-projection trajectories, and compared with k-space encoded spin echo imaging schemes collected on identical samples under equal bandwidths and acquisition timing conditions.
Results In all cases assayed, the fully refocused spatiotemporally encoded experiments evidenced a ca. 50 % reduction in signal dephasing in the proximity of the metal, as compared to analogous results stemming from the k-space encoded spin echo counterparts.
Conclusion The results in this study suggest that SPEN-based acquisition schemes carry the potential to overcome strong field inhomogeneities, of the kind that currently preclude high-field, high-resolution tissue characterizations in the neighborhood of metallic implants.

Keywords Metal-implant artifacts · Field inhomogeneities · High-definition MRI · Spatiotemporal encoding · Frequency-swept pulses · Fully refocused acquisitions

Abbreviations

MRI	Magnetic resonance imaging
NMR	Nuclear magnetic resonance
FOV	Field of view
RO	Readout
PE	Phase-encode
SS	Slice-select
SPEN	SPatio-temporal ENcoding
BP	Back-projection
RF	Radio frequency
TE	Echo time
FID	Free induction decay
FT	Fourier transform

Introduction

Many orthopedic fractures and joint problems are treated with the help of metallic implants [1]. While the

Electronic supplementary material The online version of this article (doi:10.1007/s10334-012-0318-7) contains supplementary material, which is available to authorized users.

N. Ben-Eliezer · E. Solomon · L. Frydman (✉)
Chemical Physics Department, Weizmann Institute of Science, 76100 Rehovot, Israel
e-mail: lucio.frydman@weizmann.ac.il

E. Harel
Chemistry Department, Northwestern University, Evanston, IL 60201, USA

N. Nevo
Biological Regulation Department, Weizmann Institute of Science, 76100 Rehovot, Israel

Published online: 29 June 2012

mechanical status of such implants can be monitored via standard radiographic and computerized tomography techniques, complications arise when ailments accompany this kind of implants. Such complications usually involve inflammation or other kinds of softtissue reactions that are more difficult to diagnose by strongly penetrating imaging techniques like X-rays [2]. Given magnetic resonance's superiority in characterizing water-rich tissues, this modality could serve as a method of choice in such cases. Magnetic resonance imaging (MRI), however, is significantly challenged by the severe spatial distortions of the magnetic field that metals—including non-magnetic ones—induce in their vicinity [3], and as a result often lacks radiological usefulness in the diagnosis of these ailments. Invasive modalities, including surgery and the injection of radio-sensitive contrast media, thus remain as the main available options for obtaining suitable orthopedic diagnoses in such cases.

In view of these challenges, numerous routes have been explored and exploited over the years to improve MRI's ability to characterize tissues surrounding metals [4–7]. One of the most straightforward of these approaches involves the use of spin echoes [8]. Additional avenues involve constant-time phase-encoding approaches, and the use of high intensity gradients that can partially overcome the metal-driven field distortions. Although conceptually simple, all these routes eventually face limitations stemming from the facts that spin echoes carry their refocusing solely for one instant of the data acquisition process; from the relative inefficiency with which fully phase-encoded approaches collect their data; or from the eventual limits that gradient strengths can reach to overcome the field distortions. In view of all this, a number of imaging techniques, tailored specifically for performing MRI in the neighborhood of metals, have been proposed and demonstrated. These include the use of ultrashort echo times [9], View-Angle-Tilting methods [10], Slice Encoding for Metal Artifact Correction sequences [11], metal artifact reduction sequences [12], and field-mapped based post-processing algorithms [13]. The resulting protocols offer improved immunity to field distortions, and can provide diagnostic capability under conditions that until recent years would have been considered overtly challenging.

Notwithstanding these improvements, the proximity of metallic objects to the targeted region of interest (ROI) is still a challenging, open problem in MRI. Indeed, beyond the kind of image distortions that could eventually be corrected by field mapping and post-processing, all imaging protocols reach a limit beyond which they are not able to deliver any spatial insight. This limit is usually associated with intravoxel dephasing that over the course of a signal acquisition period is simply too strong to yield observable signals, or to an intense signal pileup that cannot be deconvolved by post-processing. An alternative imaging approach has emerged in recent years, relying on imparting a spatiotemporal—rather than the conventional *k*-space—encoding [14]. Initially developed as a generic approach for acquiring 2D NMR spectra within a single scan [15, 16], this method termed *sp*atial or *sp*atiotemporal *en*coding (abbreviated henceforth as *SPEN;* see Supplementary Material available on-line for clarification of this nomenclature), was shown to be highly useful in the context of ultrafast (i.e., single-shot) 2D MR imaging, where it offers a high robustness to field inhomogeneities when compared to standard EPI [17–19]. When considered in an imaging setting SPEN utilizes a frequency-swept excitation or refocusing pulse [20]; as originally discussed by Pipe [21], one of the most interesting features of such form of encoding is the ensuing sequence's ability to specifically excite, refocus and read different locations within the sample as a function of time. SPEN can thus be used to implement a "full refocusing" scheme, whereby static T_2^* effects are refocused throughout each and every time point of the acquisition process – and not just at the echo center as in *k*-space encoding. This provides a signal enhancement without the need for any a priori knowledge of the B_0 field distribution—an information that, if available, can still be used at a post-processing stage to realign the image voxels into their undistorted positions [19].

In view of these promising features, the present study explores the feasibility of employing spatiotemporal encoding for dealing with the extreme field distortions that arise in the neighborhood of metallic objects. To this end, a number of new multi-shot SPEN protocols were implemented, and then tested on both phantom and in vivo mouse models. The resulting images were subsequently compared to images obtained using conventional spin echo MRI analogues, while paying particular attention to keeping the bandwidth and timing of all experiments as similar to one another as possible.

Materials and methods

Theoretical considerations

As detailed descriptions of the principles underlying spatiotemporal-encoding can be found in [14, 18, 19], we circumscribe this paragraph to analyzing the new pulse-sequences that were implemented in this study for dealing with extreme field inhomogeneities. The analysis will assume that SPEN was implemented along the object's *y*-axis while under the action of a general field inhomogeneity $\Delta\omega(\mathbf{r})$. As explained in further detail in the literature, SPEN is based on imparting a sequential excitation of the spins in the presence of a constant gradient G_{exc}.

Neglecting for simplicity the effects of chemical shift offsets, this endows spins with a rotating-frame frequency $\omega = \gamma G_{exc} y + \Delta\omega(\mathbf{r})$. As the offset being swept will recognize spins according to their frequency—rather than according to their position—it is convenient to redefine positions according to a $y \rightarrow \hat{y} - \frac{\Delta\omega(\mathbf{r})}{\gamma G_{exc}}$ coordinate transformation. Disregarding irrelevant constant-phase terms, this excitation scheme leads to a space-dependent quadratic phase profile equal to

$$\phi_{exc}(\hat{y}) = \frac{\gamma^2 G_{exc}^2}{2R}\hat{y}^2 - \frac{\gamma^2 G_{exc}^2 L_y}{2R}\hat{y} \tag{1}$$

where L_y is the target field of view (FOV), $R = \gamma G_{exc} L_y / T_{exc}$ is the frequency sweep rate (in units of frequency/time) of an RF pulse that has been calibrated to excite all spins spanning a FOV $\left[-L_y/2 \ldots + L_y/2\right]$ over a time T_{exc}, and γ is the gyromagnetic ratio. This expression is akin to that presented in the literature [20–22], apart from the aforementioned $y \rightarrow \hat{y}$ distortion of the spatial coordinate. SPEN relies on the explicit quadratic phase-dependence in Eq. (1), to reconstruct the spins' density profile $\rho(y)$ by reading out the free induction decay (FID) signal in the presence of an acquisition gradient G_{acq}. This can be carried out directly and without using a Fourier Transform (FT), owing to the fact that signals associated with a parabolic phase profile will only reflect the contribution of a single stationary point at which the phase's spatial derivative vanishes [23]. For all other regions, spins exhibit rapid phase variations, hence interfere destructively within their neighborhoods. Considering for concreteness our reliance on a spin echo process which reverses the phase evolution prior to detection, the resulting phase, reflected during the signal acquisition as a function of time, is given by

$$\Phi_{FID}(y,t) = -\phi_{exc}(\hat{y}) + \left[\gamma G_{acq} y + \Delta\omega(\mathbf{r})\right] \cdot t \tag{2}$$

The stationary phase approximation

$$\frac{\partial}{\partial y}\left[\Phi_{FID}(y,t)\right]_{y=\hat{y}(t)} = 0 \tag{3}$$

can be then used to reveal which voxels will be observed as a function of time yielding,

$$\hat{y}(t) = \frac{L_y}{2} - \left[\frac{\gamma G_{acq} + {}^{d(\Delta\omega)}/_{dy}}{\gamma G_{exc} + {}^{d(\Delta\omega)}/_{dy}}\right]\frac{L_y}{T_{exc}}t \tag{4}$$

The resulting signal can be now expressed as,

$$S(t) \propto \rho(\hat{y}(t)) e^{i\Phi_{FID}(y,t)} \tag{5}$$

reflecting the space–time correlation that is inherent to SPEN imaging. An explicit expression for the signal phase Φ_{FID} can be calculated by substituting Eq. (4) in the overall phase term given in Eq. (2) to yield,

$$\Phi_{FID}(t) = -\frac{\gamma G_{exc} L_y}{2T_{exc}}\left[\frac{\gamma G_{acq} + {}^{d(\Delta\omega)}/_{dy}}{\gamma G_{exc} + {}^{d(\Delta\omega)}/_{dy}}\right]^2 t^2 + \frac{\gamma G_{acq} L_y}{2}t - \left(1 - \frac{G_{acq}}{G_{exc}}\right)\cdot F(\Delta\omega) \tag{6}$$

where $F(\Delta\omega)$ denotes a function depending solely on the $\Delta\omega$ inhomogeneity offsets. Equation (6) implies that the spin dephasing we are trying to avoid can be circumvented altogether by carrying out the acquisition using $G_{exc} = G_{acq}$. Under this "full-refocusing" condition the spins' evolution will not reflect the effects of $\Delta\omega$ at any point throughout the FID, and not just at a single time point, as in a conventional spin echo. With this gradient condition given, Eq. (4) can be then used to determine the total acquisition time T_{acq} that t should take, in order to unravel the full FOV L_y : $T_{acq} = T_{exc}$. Notice, however, that despite eliminating explicit $\Delta\omega$ dependence from the overall spin evolution, the resulting image is still not free from the effect of field inhomogeneities, which will be reflected in the reconstructed $\rho(\hat{y})$ profile, as a distortion of the voxel's positions according to the $y \rightarrow \hat{y} - \frac{\Delta\omega(\mathbf{r})}{\gamma G_{exc}}$ transformation. As mentioned, this effect can be traced to the frequency distortions that the inhomogeneity will make on the voxels away from their ideal γGy frequency values. However, as both the excitation and the acquisition processes use similar gradient strengths, identical shifts in the coordinate axis will take place in both cases, and these can be thus deconvolved by remapping the reconstructed images based on ancillary measurements of the field inhomogeneities [19]. Also interesting to highlight is the fact that deviations in the linearity of the effective gradients will also affect the point-spread function—and therefore to some extent also the voxels' sizes—throughout the targeted FOV. All this being said, the strength of this approach still remains in the fact that SPEN is able to *fully compensate, throughout the entire acquisition*, for the dephasing effects imparted by the $\Delta\omega$ evolution.

MRI Sequences

To test the performance of fully refocused SPEN under extreme field inhomogeneities, two multi-shot SPEN sequences were implemented and compared versus conventional spin echo analogues. The first sequence variant replaced the frequency encoding along a readout (RO) dimension with a fully refocused SPEN (oriented along the images' vertical y-axis). The refocusing π-pulse in this sequence was implemented in a band-selective fashion to provide slice selectivity along the z-direction, while phase-encoding (PE) was applied in a constant-time fashion to encode positions along the horizontal x-axis (thereby

eliminating in essence most distortions along this dimension). The resulting 2D SPEN spin echo sequence is illustrated in Fig. 1b, as compared to a conventional 2D spin echo analogue shown in Fig. 1a. Typical echo times (TE) and other parameters assayed with both sequences are summarized in the Figure's legend. Notice that for the sake of consistency very similar timing and bandwidth (i.e., gradient) values were utilized in the initial excitation stages for both sequences; identical parameters were then used in all remaining parts of the sequences, in sense of gradients, timing, bandwidth, resolution and FOV. Notice as well that although an interleaved multi-slice operation is in principle possible in SPEN-based experiments [27], the spin echo version illustrated in Fig. 1a can readily perform such multi-slice acquisitions whereas its SPEN counterpart in panel b is slice-selective but not optimized for multi-slice acquisitions.

A second set of sequence variants is shown in Fig. 1c–d, and is designed based on radial back-projection (BP) sampling. The rationale in employing this scheme was that while PE offers the most straightforward imaging alternative when dealing with small field distortions, BP—scanning its data either purely in *k*-space or by SPEN—might be a better option to highlight the performance differences between the two encoding methods. Moreover, BP provides a more suitable starting point when eventually facing extremely short T_2^* values—not only in dealing with metal implants, but also when contemplating solid state NMR or EPR imaging experiments. Two comparable back-projected schemes where thus evaluated in this study: one involving a conventional spin echo (Fig. 1c) and the other a SPEN-based spin echo (Fig. 1d) scheme. In both cases, a series of 1D radial readouts were used to encode the image information—either in the frequency/*k*-space domain, or

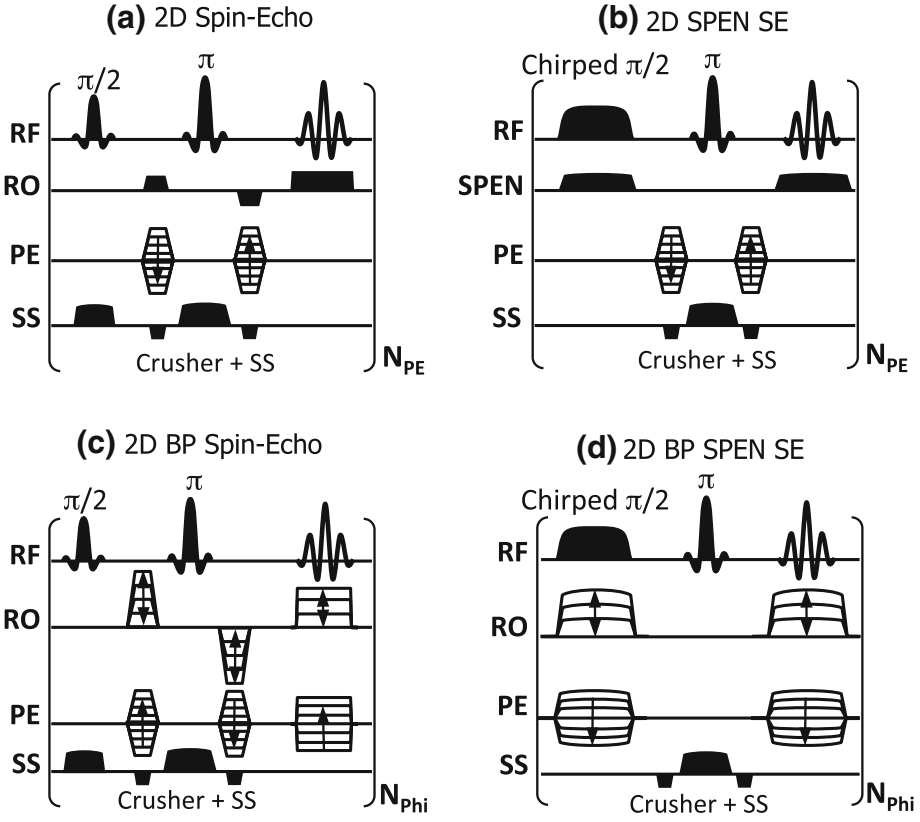

Fig. 1 Multi-shot 2D MRI pulse sequences compared in the present study. **a**, **b** Conventional *k*-encoded spin echo and new SPEN-based spin echo sequence proposed in this study. In the experiments described below, both sequences were implemented with $N_{pe} = 128$ phase-encoding steps; additional parameters included TR = 200 ms, slice-thickness = 1 mm along the 3rd (SS) dimension achieved using 4 ms band-selective π refocusing pulse, acquisition time = 2.56 ms, acquisition bandwidth = 125 kHz. Excitations used a 2 ms $\pi/2$ pulse for the *k*-space sequence, and a 2.56 ms $\pi/2$ chirped pulse sweeping over 102 kHz for the SPEN sequence. The acquisition gradient was $G_{RO} = 9.78$ G/cm for **a**, and $G_{exc} = G_{acq} = 8$ G/cm along the SPEN axis for **b**. **c**, **d** Back-projection analogues tested to compare the respective performances of *k*- and SPEN-based sequences. In these instances $N_{phi} = 180$ projections were taken; remaining parameters were similar to the ones used in panels (**a**) and (**b**). Image reconstruction included: **a** 2D FT, **b** 1D FT along the PE and a super-resolved reconstruction along the SPEN dimension [23], **c** 1D FT along the RO dimension followed by a common BP reconstruction of the resulting data set, **d** super-resolved reconstruction along the SPEN dimension followed by a common BP reconstruction of the resulting data set

directly in *r*-space in the SPEN acquisitions. These were then subjected to 1D reconstruction using FT for the *k*-space experiments and super-resolution reconstruction for the SPEN experiments; subsequent processing involved applying the same projection-reconstruction scripts to both sets of data. As this implies, being devoid from a PE dimension that is substantially more immune to inhomogeneities than other forms of encoding, and owing to the use of the same number of radial projections that were subject to identical reconstruction algorithms, this comparison provides a reliable metric on the relative merits of the two encoding modes here evaluated.

Experimental and post-processing methods

All experiments were performed at 7 T on a 300/89 Varian VNMRS vertical microimaging system (Varian Associates, Inc., Palo Alto, CA, USA) using a quadrature-coil probe with a FOV of $30 \times 30 \times 46$ mm^3. Three samples were examined in the study: (1) A plastic cross-shaped phantom placed inside a 25 mm diameter tube filled with tap water and containing a stainless steel rod ca. 1.5 mm in diameter running through its center. (2) Two concentric glass tubes 20 and 5 mm in diameter placed in agar gel and containing a stainless steel rod. (3) In vivo mice, with a titanium disc ($\approx$3 mm thick, 8 mm in diameter) attached to their skull. Animal experiments were carried out on healthy SCID mice, and handling was done in accordance with protocols approved by the Weizmann Institute's Animal Care and Use Committee. In order to simulate and assess the effects of a metallic implant, the animal's head was shaved and a titanium disc was externally attached to the mouse skull. All sequences were written in C-language and are available upon request. Post-experimental data processing was implemented using custom-written MATLAB® (The MathWorks, Inc., Natick, MA, USA) software packages, also available upon request. Image reconstruction was done by applying conventional Fourier Transformation along the *k*-space encoded dimensions (whether PE or RO), and using the super-resolution reconstruction algorithm presented in Ref. [24] for processing SPEN data, with typical super-resolution enhancement factors of 2. The radial based sequences in Fig. 1c, d were subsequently subjected to back-projection reconstruction, using MATLAB based functions.

Results

Phantom investigations

Figure 2a, b present a series of phantom images acquired using the conventional and the SPEN-based 2D spin echo Cartesian schemes, shown respectively in Fig. 1a, b. Images were collected as a function of position along the slice-selective *z*-axis. A metal-derived artifact is clearly visible, particularly in the neighborhood of the $z = 0$ mm position, for which the rod-derived field distortion is maximal. None of the assayed sequences is capable of eliminating these strong effects, at least for the set of parameters (i.e., gradient strengths, TEs) that were used. For the remaining positions, however, it is clear that the SPEN-based sequence produced fewer distortions than its *k*-space based counterpart – despite the latter sequence's reliance on slightly higher bandwidths and shorter TEs than those used by SPEN. The nature of the metal-derived distortions are in fact of somewhat different appearance at these $z \neq 0$ positions, with a more noticeable piling-up of the signal intensity around the metal rod in the SPEN-derived images versus a metal-derived signal void in the conventional spin echo. This is a manifestation of the full-refocusing ability of SPEN, when coping with intravoxel T_2^*-like decays.

Figure 3a, b present a second set of comparisons using the same phantom, this time based on back-projected imaging (sequences shown in Fig. 1c, d respectively). The resulting comparison shows an improved performance of the spatiotemporal-encoding scheme over its conventional counterpart. Although streaking artifacts (characteristic of using a limited number of projections) are apparent in both sets of data, they are much less substantial in the SPEN than in the *k*-derived images. As in the Phase-Encoded results shown in Fig. 2, signal pile-up is more generally evidenced in the SPEN-based images, as compared to signal voids seen in the *k*-space encoded ones.

An additional evaluation of the PE and BP sequences illustrated in Fig. 1 was done on phantom composed of a stainless-steel metallic rod placed in-between agar-separated concentric test tubes. The overall behavior observed in these tests was similar to that already presented in Figs. 2 and 3 and hence it is not explicitly shown; these data are available upon request.

In vivo measurements

A series of in vivo scans performed on a healthy mouse with a titanium disc attached are shown in Fig. 4. Axial images arising from this construct (pictured on the right), clearly evidence the distortions that this object imparts on this vertically positioned animal; particularly directly underneath the disc, and for a depth of ca $\Delta z \approx 5$ mm into the head. Similar to the phantom models, remarkably weaker signal dephasing effects are noticed in the spatio-temporally encoded images (Fig. 4, bottom), as compared to their conventional spin echo counterparts (Fig. 4, top). In the latter case, both the skin and the topmost 3 mm brain regions are missing, due to the presence of the metal disc

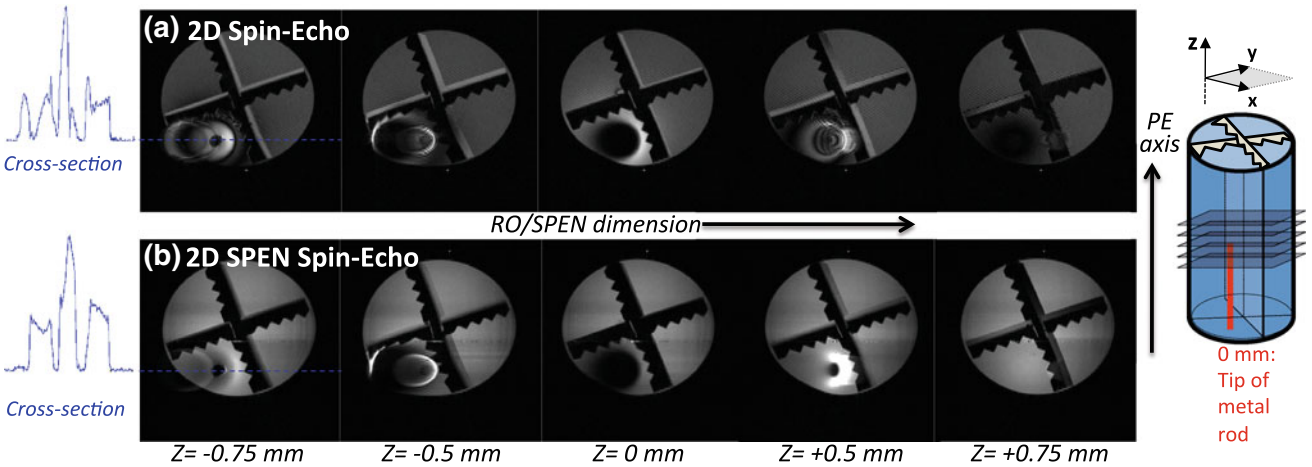

Fig. 2 Comparison of multi-shot MR images of a metal-implanted cross-shaped phantom shown at the right side of the figure and using a Cartesian sampling scheme. **a** Results obtained from the *k*-space encoded spin echo sequence illustrated in Fig. 1a; **b** Idem for the SPEN-based sequence illustrated in Fig. 1b. Slices along the vertical *z* direction were selected at the indicated positions by changing the offset of the slice-selective RF pulses in the sequences. In both data sets **a** and **b** FOV = 30 × 30 mm^2; spatial resolution = 0.23 × 0.09 mm^2 (along the PE × RO dimensions respectively). Other experimental parameters are as delineated in Fig. 1. Cross-sections on the left illustrate representative comparisons of each sequence's immunity to metal-induced distortions, as judged by 1D profiles taken at the indicated *dashed lines*

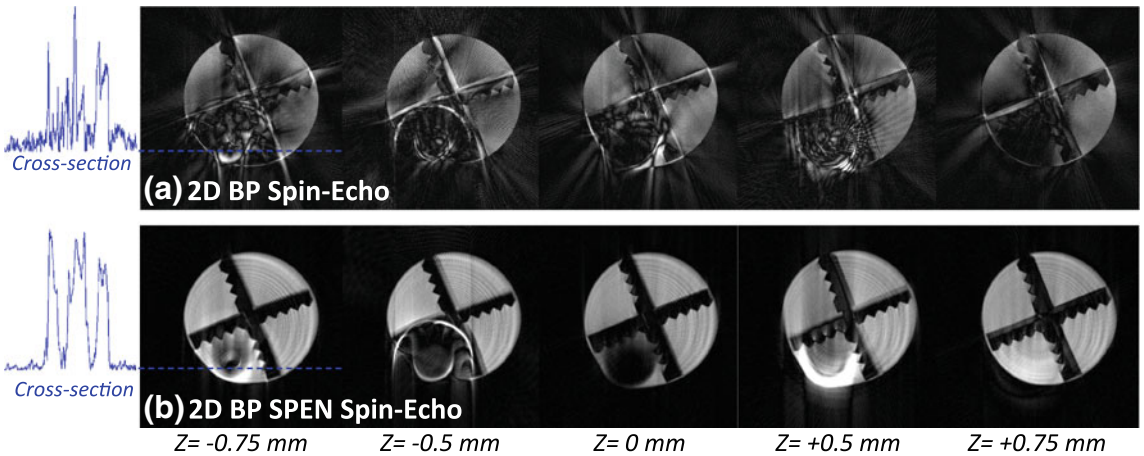

Fig. 3 Idem as in Fig. 2, but upon utilizing the back-projected sequence variants introduced in Fig. 1c, d. Projections were performed by varying the *x*- and *y*-gradient strengths so as to provide constant angular increments of 1°; strengths and timings were set to yield a 0.09 mm spatial-resolution for each of these radial projections

(artificially superimposed on the processed images for illustrative purposes). By contrast, apart from minor weakening and distortion of the signal in some of the *z* slices, the SPEN-based images provide faithful reconstruction of both the brain, and of the skin tissues throughout the imaged FOV. Similar results were produced upon collecting sagittal images on the same construct (images not shown).

Even more significant were the differences arising upon employing the 2D back-projection radial imaging sequences on this in vivo model (Fig. 5). In this case the distortions and signal voids in the *k*-space encoded images appear to propagate to an even farther, distal region of the brain. By contrast, only slight deformations affect the spatiotemporally encoded images. Streaking artifacts appear in both data sets shown in Fig. 5, and are related to a certain measure of angular undersampling *vis-à-vis* the back projection reconstruction scheme that was used. These can be avoided by increasing the number of projections or by using more advanced BP processing procedures.

The cross-sections illustrated in Figs. 2, 3, 4, 5 are meant to give qualitative depictions on the relative merits of the SPEN versus the spin echo approaches, for scanning a targeted region in the neighborhood of the metals. A complementary, semi-quantitative depiction of the

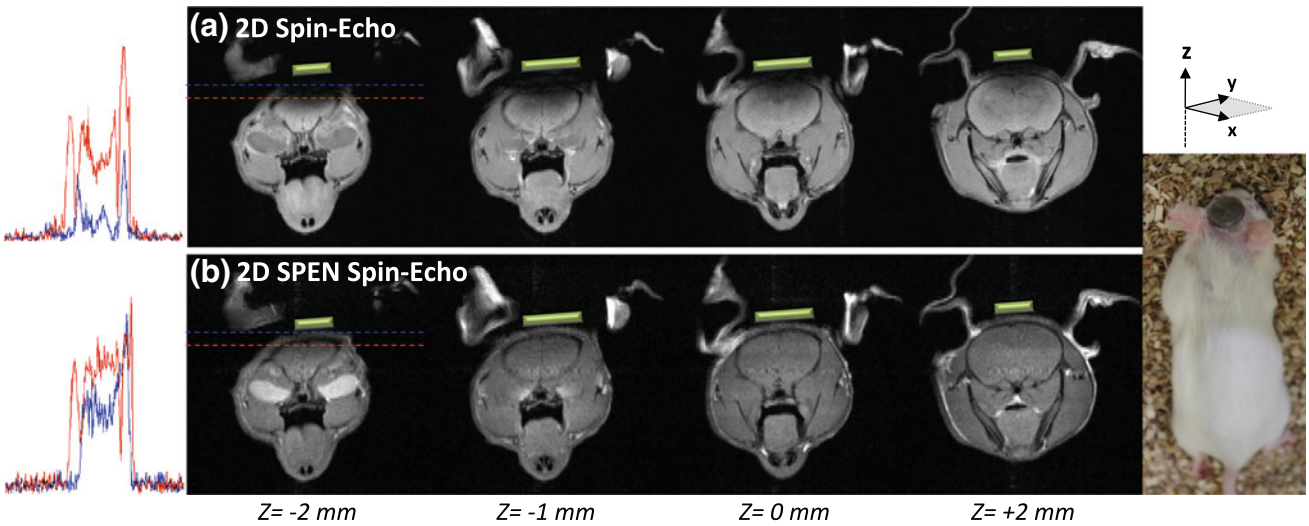

Fig. 4 2D Cartesian sampled images of a mouse head, to which a ca. 3 mm thick × 8 mm in diameter Titanium disc has been attached (picture shown on the *right*). For illustrative purposes, images were artificially superimposed with the approximate location of the disc. **a** Results stemming from the *k*-space based sequence illustrated in Fig. 1a. **b** Idem for the SPEN-based sequence illustrated in Fig. 1b. Scan parameters are identical to those involved in Fig. 2. Cross-sections on the *left* illustrate representative comparisons of each sequence's results in regions neighboring the metal implant, as judged by 1D profiles taken at the indicated *dashed lines* (red profile at *red line*, blue profile at *blue line*). The differing intensities exhibited by sets of images for the more distal regions of the head—e.g., for the eye orbits in the $Z = -2$ mm slice—are reflective of the sequences' differing contrast mechanisms (stemming in particular from the bulk versus selective nature of the sequences' respective excitation pulses)

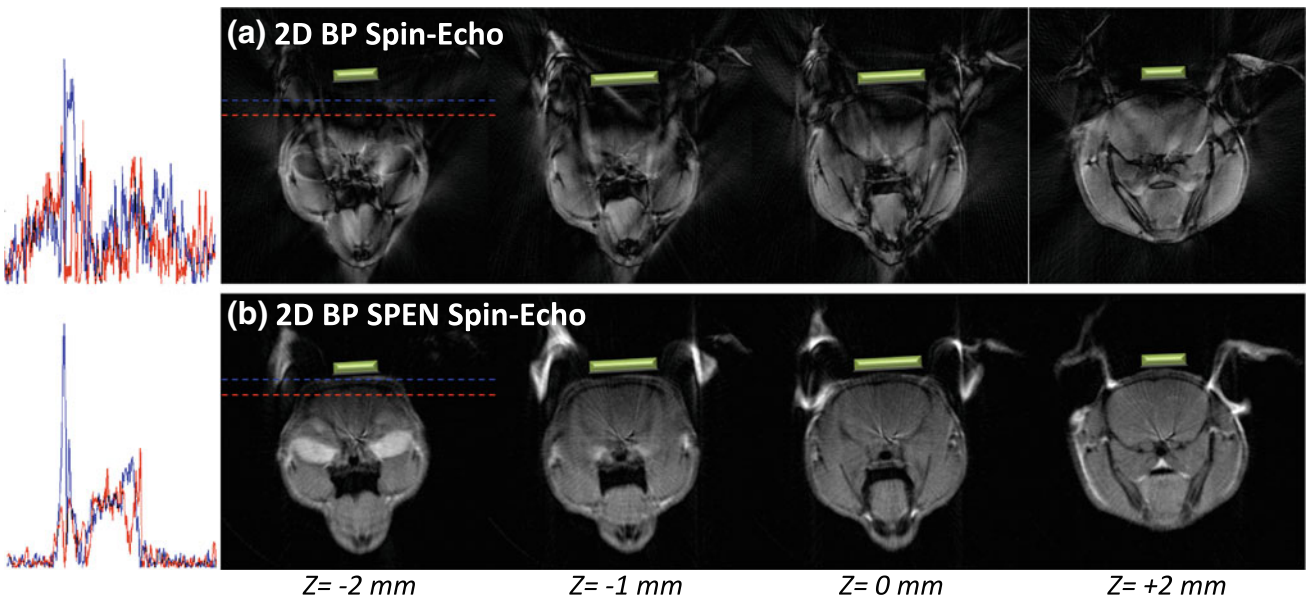

Fig. 5 2D back-projection images of a mouse head, attached with a Titanium disc as shown in Fig. 4. **a** *k*-space based sequence illustrated in Fig. 1c. **b** SPEN-based sequence illustrated in Fig. 1d. Scan parameters are identical to those involved in Fig. 3; cross-sections were taken at the illustrated positions

former's higher immunity to metal-derived distortions, follows from the plots given in Fig. 6. These plots illustrate, for the in vivo experiments introduced in Figs. 4 and 5, the relative intensities of voxels proximate to the metal artifact, after normalization by the integrated intensity displayed by equal-area voxels positioned far away form the metal. As can be seen, for the two kinds of acquisition schemes introduced in Fig. 1 (phase-encoded and BP), the spatiotemporally encoded images display relative intensities that in the proximity of the metal implant are between 50 and 100 % higher than those evidenced by their spin echo counterparts.

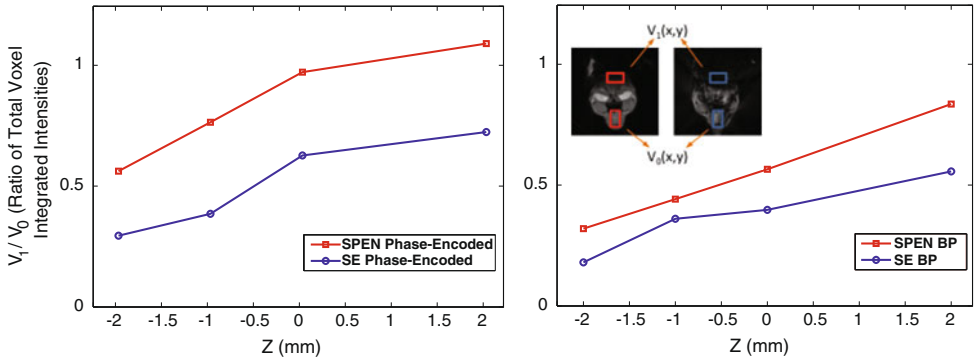

Fig. 6 Relative integrated intensities evidenced by the 2D in vivo images introduced in Figs. 4 and 5, for 2.5 × 4 mm voxels $V_1(x,y)$ positioned in the proximity of the metal disk, after normalization by the integrated intensities of analogous reference voxels V_o positioned in the indicated *distal* regions. (*Left*) Results arising from the phase-encoded experiments. (*Right*) Idem but for the back-projected data. The same voxel positions V_o, V_1 were taken for analyzing both sets of imaging data. Notice the higher relative ratios afforded by the SPEN-based acquisitions (*red lines*) for all examined *Z* slices, over their conventional spin echo counterparts (*blue lines*)

Discussion

While originally developed as a general method for collecting multidimensional NMR spectra within a single-scan, SPEN was also shown to have significant merits in the field of MR imaging. Notwithstanding these recent developments, similar encoding schemes were previously investigated by Kunz, Pipe, Wong, Chamberlain, Shen and co-workers, all of whom made use of frequency-swept pulses for the spins' excitation [17, 20, 21, 25, 26]. The present study extends those earlier and our recent investigations, to a more generic multi-shot context geared at exploiting SPEN's inherent refocusing capabilities. By equating the bandwidth and duration of SPEN's excitation and acquisition processes, it is possible to generate a special spin echo that refocuses T_2^* dephasing throughout the course of the data acquisition, and allows collecting images under conditions that clearly limit the use of conventional *k*-space based spin echo imaging techniques. While no prior knowledge of the field distortions or inhomogeneity maps is necessary in this case, these maps can still be exploited to correct for the smearing-out and pile-up distortions that under sufficiently large inhomogeneities still affect the SPEN images due to the aforementioned $y \rightarrow \hat{y}$ displacements.

The choice of comparing Cartesian-based standard 2D spin echo and spatiotemporally encoded variants was driven by the former sequence's widespread use in 2D imaging. Although shorter TEs could have been probed upon setting up the experimental parameters used in Figs. 2 and 4, the selected values were chosen so as to obtain adequate spatial resolutions while corresponding to the kind and size of inhomogeneities that were being dealt with. For this choice of parameters, the superiority of SPEN readouts over their conventional *k*-space counterparts appeared very clearly. We envision that this superior performance will remain valid, so long as the $\gamma \Delta B_o TE$ product remains within the kind of unity values that were hereby examined. Still, as field inhomogeneities grow increasingly larger, one can expect the performance of the π pulses, common to both encoding techniques, to degrade. Eventually, it is plausible that sufficiently large inhomogeneity values will even complicate the gradient-switching delays involved in these pulse sequences, thus preventing the implementation of both the classical spin echo as well as of the slice-selective spin echo involved in the fully refocused SPEN sequence. To deal with such instances we decided to extend the comparison among the relative merits of *k*-space versus SPEN sequences to a different class of experiments – this time involving radial back-projection. As in the Cartesian case, the resulting images (presented in Figs. 3, 5) provide strong evidence favoring the use of SPEN. A further aspect of the BP scheme is that the frequency-swept pulses can be used not only for the $\pi/2$ but also for implementing the π refocusing events [17]; in such instance, no gradient switching events would have to be involved altogether. The resulting sequence is thus expected to be highly robust – even against field inhomogeneities that are larger than the ones hereby probed.

Notwithstanding these promising results and the prospects to extend them to volumetric MRI, a number of issues should be considered when moving forward towards clinical applications. One of these is the inherent reliance of SPEN on frequency-swept pulses. These result in a bulk $\pi/2$ excitation of all spins in the sample, thereby limiting the use of short TR for slice interleaving, and hampering fast volumetric coverage when multi-slice 2D protocols are employed. In a recent report we described a number of approaches that can be used to alleviate this constraint (such as the application of storage pulses, or the use of PE along the 3rd dimension), enabling rapid scanning of a third dimension at no additional scan-time costs [27].

Another essential aspect of SPEN relates to specific absorption rate (SAR) restrictions; in particular considering its repeated use of frequency swept pulses, and the putative presence of metals capable of concentrating the radiation effects [28]. These issues are currently being explored with a number of alternatives including the use of multi stationary points, parallel receive protocols, and small-angle excitations. The feasibility of extending these concepts towards imaging different classes of fast-relaxing systems like those arising in solid state NMR and in EPR, is also under investigation.

Conclusion

Previous studies had shown the potential opened up by spatio-temporal encoding methods, towards the robust acquisition of MR images in a single scan. The present work extends these SPEN-based imaging concepts by showing that superior multi-shot spin echo images can arise from SPEN data collected under fully refocused conditions. Indeed, by contributing to a refocusing of T_2^* effects *throughout* the signal acquisition process—instead of at a single instant τ as happens in conventional spin echoes—these methods were found to be particularly helpful for dealing with otherwise intolerable field distortions. These characteristics were demonstrated in the present work within the context of restoring image faithfulness in the proximity of external metal objects; such restoration was clearly evidenced in both phantom- and animal-based models. Additional work is currently in progress, to explore the potential of these advantages within the context of radiological investigations in the neighborhood of human metallic implants. Moreover, we envision that similar advantages can be brought to bear in high-field investigations of other regions where magnetic field homogeneities are challenged, including high-field instances dealing with rapid changes in susceptibility driven by air/tissue interfaces.

Acknowledgments E. Harel acknowledges support from the Institute for Complex Adaptive Matter Branches Cost-Sharing Fund. This research work was supported by the Israel Science Foundation (ISF 447/09), the Minerva Foundation (Project 710587; Federal German Ministry for Education and Research), a Helen and Kimmel Award for Innovative Investigation, and by the generosity of the Perlman Family Foundation.

References

1. Goitz HT, Goitz RJ, Watson JT, Schurman JR, Herbert J, Roth HJ (1996) Orthopedic implants: a guide to radiographic analysis. Curr Probl Diagn Radiol 25(4):109–168
2. Griffiths HJ (1995) Imaging of orthopedic hardware. W.B. Saunders Co, Philadelphia. Radiologic clinics of North America Series 33(2)
3. O'Donnell M, Edelstein WA (1985) NMR imaging in the presence of magnetic field inhomogeneities and gradient field nonlinearities. Med Phys 12(1):20–26
4. Jung KJ, Moon CH (2009) Effect of slice angle on inhomogeneity artifact and its correction in slice-selective MR imaging. Concept Magn Res Part A 34A(4):238–248
5. Koch KM, Hargreaves BA, Pauly KB, Chen W, Gold GE, King KF (2010) Magnetic resonance imaging near metal implants. J Magn Reson Imaging 32(4):773–787
6. Suh JS, Jeong EK, Shin KH, Cho JH, Na JB, Kim DH, Han CD (1998) Minimizing artifacts caused by metallic implants at MR imaging: experimental and clinical studies. Am J Roentgenol 171(5):1207–1213
7. Viano AM, Gronemeyer SA, Haliloglu M, Hoffer FA (2000) Improved MR imaging for patients with metallic implants. Magn Reson Imaging 18(3):287–295
8. Tartaglino LM, Flanders AE, Vinitski S, Friedman DP (1994) Metallic artifacts on mr-images of the postoperative spine—reduction with fast spin echo techniques. Radiology 190(2):565–569
9. Robson MD, Gatehouse PD, Bydder M, Bydder GM (2003) Magnetic resonance: an introduction to ultrashort TE (UTE) imaging. J Comput Assist Tomogr 27(6):825–846
10. Cho ZH, Kim DJ, Kim YK (1988) Total inhomogeneity correction including chemical shifts and susceptibility by view angle tilting. Med Phy 15(1):7–11
11. Lu W, Pauly KB, Gold GE, Pauly JM, Hargreaves BA (2009) SEMAC: slice encoding for metal artifact correction in MRI. Magn Reson Med 62(1):66–76
12. Koch KM, Lorbiecki JE, Hinks RS, King KF (2009) A multispectral three-dimensional acquisition technique for imaging near metal implants. Magn Reson Med 61(1):381–390
13. Lai CM (1983) Reconstructing NMR images from projections under inhomogeneous magnetic field and non-linear field gradients. Phy Med Biol 28(8):925–938
14. Shrot Y, Frydman L (2005) Spatially encoded NMR and the acquisition of 2D magnetic resonance images within a single scan. J Magn Reson 172(2):179–190
15. Frydman L, Scherf T, Lupulescu A (2002) The acquisition of multidimensional NMR spectra within a single scan. Proc Natl Acad Sci USA 99(25):15858–15862
16. Shrot Y, Frydman L (2003) Single-scan NMR spectroscopy at arbitrary dimensions. J Am Chem Soc 125(37):11385–11396
17. Chamberlain R, Park JY, Corum C, Yacoub E, Ugurbil K, Jack CR Jr, Garwood M (2007) RASER: a new ultrafast magnetic resonance imaging method. Magn Reson Med 58(4):794–799
18. Tal A, Frydman L (2006) Spatial encoding and the single-scan acquisition of high definition MR images in inhomogeneous fields. J Magn Reson 182(2):179–194
19. Ben-Eliezer N, Shrot Y, Frydman L (2010) High-definition, single-scan 2D MRI in inhomogeneous fields using spatial encoding methods. Magn Reson Imaging 28(1):77–86
20. Kunz D (1986) Use of frequency-modulated radiofrequency pulses in MR imaging experiments. Magn Reson Med 3(3):377–384
21. Pipe JG (1995) Spatial encoding and reconstruction in MRI with quadratic phase profiles. Magn Reson Med 33(1):24–33
22. Tal A, Frydman L (2010) Single-scan multidimensional magnetic resonance. Prog Nucl Magn Reson Spectrosc 57(3):241–292
23. Guillermin V, Sternberg S (1990) The method of stationary phase. In: Geometric Asymptotics. American Mathematical Society, Mathematical Surveys and Monographs, vol 14, pp 1–16
24. Ben-Eliezer N, Irani M, Frydman L (2010) Super-resolved spatially encoded single-scan 2D MRI. Magn Reson Med 63(6): 1594–1600

25. Meyerand ME, Wong EC (1995) A time encoding method for single-shot imaging. Magn Reson Med 34(4):618–622
26. Shen J, Xiang Y (2010) High fidelity magnetic resonance imaging by frequency sweep encoding and Fourier decoding. J Magn Reson 204(2):200–207
27. Ben-Eliezer N, Frydman L (2011) Spatiotemporal encoding as a robust basis for fast three-dimensional in vivo MRI. NMR Biomed 24(10):1191–1201
28. Dempsey MF, Condon B (2001) Thermal injuries associated with MRI. Clin Radiol 56(6):457–465